Eur. Phys. J. Plus (2015) **130**: 29
DOI 10.1140/epjp/i2015-15029-1

THE EUROPEAN PHYSICAL JOURNAL PLUS

Regular Article

The effect of bias voltage on microstructure and hardness of TiN films grown by ion coating deposition

P. Balashabadi[1], M.M. Larijani[2,a], A.-A. Shokri[3], E. Jafari-Khamse[4], H. Seyedi[1], and S. Eshghi[5]

[1] Nuclear Science & Technology Research Institute, Physics and Accelerators School, Karaj, Iran
[2] Nuclear Science & Technology Research Institute, Radiation Application Research School, Karaj, Iran
[3] Department of Physics, Payamnoor University of Tehran- Shargh, Tehran, Iran
[4] Department of Physics, University of Kashan, Kashan, Iran
[5] Department of Materials engineering, Tehran Science and Research Branch, Islamic Azad University, Tehran, Iran

Received: 22 April 2014 / Revised: 14 November 2014
Published online: 24 February 2015 –

Abstract. Titanium nitride (TiN) thin films were grown onto 316 stainless steel substrate at 350 °C by hollow cathode discharge ion plating technique. Since microstructure and mechanical properties of the samples were strongly affected by bias voltage, different bias voltages from 0 to $|-120|$ V were applied to the substrate. Rutherford back-scattering spectroscopy showed that the film thickness decreased when the bias voltage increased. X-ray diffraction patterns showed that the as-prepared TiN thin films were preferentially grown in the (200) direction with a satisfactory crystal quality at −30 V. The spatial scaling behavior of the TiN films grown by ion coating have been investigated by using the atomic force microscopy as well as a kinetic roughening model for the film thickness ranging from 380 to 590 nm. The roughness and dynamic scaling exponents have been independently measured ($\alpha = 0.7 \pm 0.05$ and $z = 3.03 \pm 0.05$) and they exhibited a smooth surface growth. Nanohardness showed formation of a film with 30 GPa hardness and 285 GPa Young modulus at −30 V bias voltage.

1 Introduction

Transition metal nitrides have been extensively used in industry as protective hard coatings because of their hardness and wear resistance. The most popular one is titanium nitride (TiN) as a hard material. It has been used in numerous applications considering its excellent corrosion and erosion resistance, high hardness [1], high melting point, low friction coefficient, thermal stability [2,3], chemical stability [4], biocompatibility [5] and desirable optical and electronic properties. Many techniques, such as magnetron sputtering [6], reactive evaporation [7], ion-beam deposition [8], ion plating [9] and chemical vapor deposition [10] have been used to grow TiN thin films. Physical vapor deposition methods, in general, involve the deposition of titanium atoms on the substrate surface by sputtering or evaporation followed by a subsequent reaction with nitrogen on the substrate surface in a moderate substrate temperature (around 300–550 °C). It was reported that the deposition parameters strongly affected the physical properties of the films, such as structure and mechanical properties [11]. Saoula *et al.* [12] studied the effect of nitrogen content and substrate bias on the composition and the structure of TiN films deposited onto silicon (100) by reactive RF magnetron sputtering at ambient temperature and low pressure. They found that the application of substrate bias effectively removes the oxygen and the carbon impurities and form stoichiometric TiN.

The kinetic roughening in the growth of thin films has scientific and technological significance. Many theoretical and experimental efforts were recently devoted to understand the growth processes and roughening mechanisms [13–15]. A variety of surfaces and interfaces associate with self-affine fractal scaling [16]. All rough surfaces exhibit perpendicular fluctuations to the surface characterized by a single valued Gaussian rough surface and root-mean-square (RMS) width. Several theoretical approaches were extended to describe films grown under non-equilibrium conditions [17].

[a] e-mail: mmojtahedzad@gmail.com

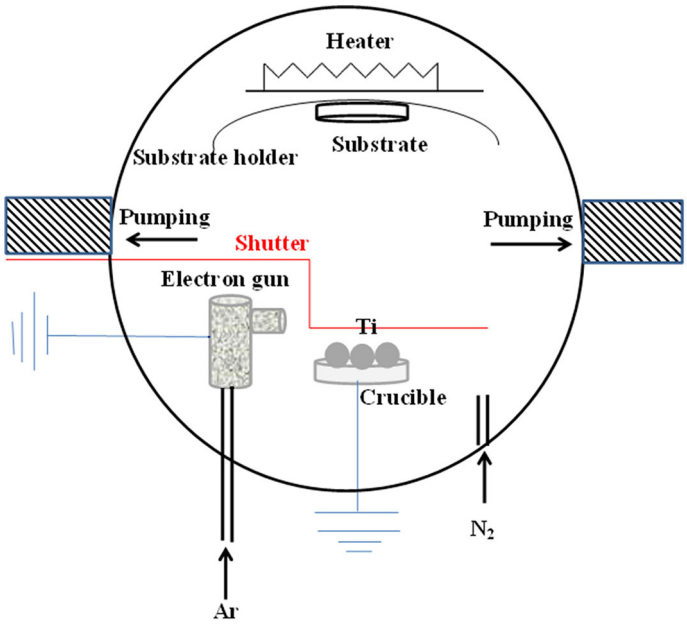

Fig. 1. Schematic diagram of the HCD-IP system.

RMS width usually has scaled with time and film thickness as follows:

$$\mathrm{RMS}(h,t) = h^{\alpha} F(t/h^{\alpha/\beta}), \quad \mathrm{RMS}(h) \sim h^{\alpha} \quad \text{for} \quad t/h^{\alpha/\beta} \to \infty, \quad \mathrm{RMS}(t) \sim t^{\beta} \quad \text{for} \quad t/h^{\alpha/\beta} \to 0, \tag{1}$$

where α and β are defined as the roughness and growth exponents, respectively, and used to characterize the nature of the surface roughness. The correlation length (ζ), the distance at which the surface features become uncorrelated, increases with the film thickness as

$$\zeta \sim h^{1/z}, \tag{2}$$

where $z = \alpha/\beta$ is the dynamic scaling exponent.

Theoretical approaches of non-equilibrium film growth employ partial differential equations of time-dependent vertical height. The Kardar-Parisi-Zhang (KPZ) [18] and the Siegret-Plischke (SP) equations [19] are two well-known examples of these theoretical approaches, in which a height-height correlation function is calculated for studying the statistical ordering behavior of the deposited films.

In this study, TiN thin films were deposited using the ion coating technique at 350 °C. The effect of negative bias voltage applied to the substrate (V_b) on the structure, composition and hardness of the films was investigated. Since surface characteristics affect the film hardness, surface roughening dynamics was quantitatively studied by a height-height correlation function.

2 Experimental details

Hollow cathode discharge ion plating (HCD-IP) was utilized to deposit TiN thin films onto mirror polished ($1 \times 1 \times 0.5\,\mathrm{cm}^3$) 316 stainless steel at 350 °C. At first, the substrates were ultrasonically cleaned in successive baths of acetone and ethanol for 20 min each followed by a final ultrasonic washing with distilled water for 10 min to remove the possible organic contaminants on the surface. After that, they were immediately inserted into a vacuum chamber for deposition. The experimental device is a stainless steel cylindrical chamber ($\varnothing = 250\,\mathrm{mm}$, $L = 400\,\mathrm{mm}$). A schematic diagram of the experimental set up is shown in fig. 1. The chamber was evacuated to the base pressure of 3×10^{-3} Pa using the rotary and diffusion pumps. Highly pure Ti granules (99.99%) were placed in a graphite crucible. Deposition was carried out with introducing the Ar (25 sccm) and N_2 gases (1 sccm) into a chamber at the working pressure of 7.2×10^{-2} Pa. Argon gas was introduced to the vacuum chamber from tip of tantalum tube (Ta) as cathode. Electrical discharge between the electrodes caused to ionize the gas and to form a plasma. Ta tube and crucible containing evaporative materials act as cathode and anode, respectively. The cathode temperature increased to 2300–2400 °K following the bombardment by positive ions resulting in emission of electrons. Maximum current and acceleration voltage of the electron beam were 120 A and 28 V, respectively. The kinetic energy of the focused beam on the anode was converted to thermal energy and vaporized the contents of the crucible. The incident electrons also caused to

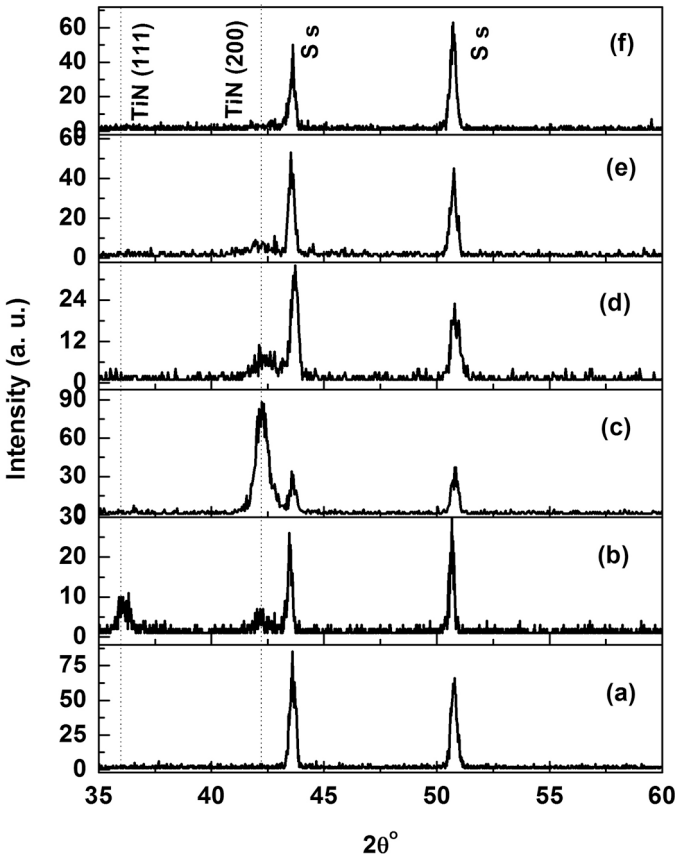

Fig. 2. XRD patterns of (a) stainless steel substrate, TiN films deposited at (b) 0, (c) −30, (d) −60, (e) −90 and (f) −120 V bias voltages.

ionize the gas between the electrodes to form a stable discharge and plasma. The cross section of the beam can be also controlled using a magnetic field. A negative substrate bias from 0 to −120 V with −30 V intervals was applied to the substrates during the growth. Some fraction of the evaporated metal atoms was ionized in the plasma via an electron beam source. After that the ions were accelerated toward the substrate by an electric field applied from an external power supply between the evaporating source and the substrate. The evaporated Ti atoms react with reactive gas to deposit as a specific compound on the substrate located on the work piece holder positioned above the hollow cathode. During coating, the substrates were placed on the holder which can be rotated around the chamber center axis by a controlled variable speed DC motor to improve homogeneity in the film thickness and composition. To avoid contamination, a metal shield above the crucible was used.

The film structure was characterized by X-ray diffraction (XRD, H2E-STOE-Germany; STIDY-MP model) patterns with monochromatic copper radiation (Cu K_α). The morphology of the deposited films was characterized by T-Scan Scanning electron microscopy (SEM, Vega2 model). Atomic force microscopy (AFM, Autoprobe CP model) was employed to determine the surface topography and the roughness of the films. Thickness and atomic composition of the as-prepared films were measured using RBS (single-ended 3 MeV Van de Graaff machine, manufactured by HV.Co) technique via the SIMNRA simulation package. The error of this technique for determination of thickness is considered ±5%. The scattered particles from a 2 MeV incident proton beam were measured by a surface barrier detector at 165° and then numerical analysis of the collected data was performed. Film hardness was estimated using a triboscope nanoindentation system (A Hysitron Inc. TriboScope, USA). X-ray photoelectron spectroscopy (XPS, TWIN ANODE XR3E2 X-RAY SOURCE SYSTEM model) analysis was performed to study the surface chemical bonding states.

3 Results and discussion

The XRD patterns of the films under various bias voltages are depicted in fig. 2. It shows characteristic diffraction pattern of pure TiN (200) preferred orientation at −30 V bias. Small peak due to (111) orientation can be observed too. Apart from the film prepared at −30 V bias, all the films present an amorphous structure. It is probably because of the momentum transfer from the ions to the deposited atoms and also thermodynamic conditions on the substrate surface which are adequate for reaction of Ti and N_2 as well as for nucleation and grain growth. Figure 3 shows typical RBS pattern of the film deposited at −30 V. The atomic ratio of titanium to nitrogen is evaluated from the

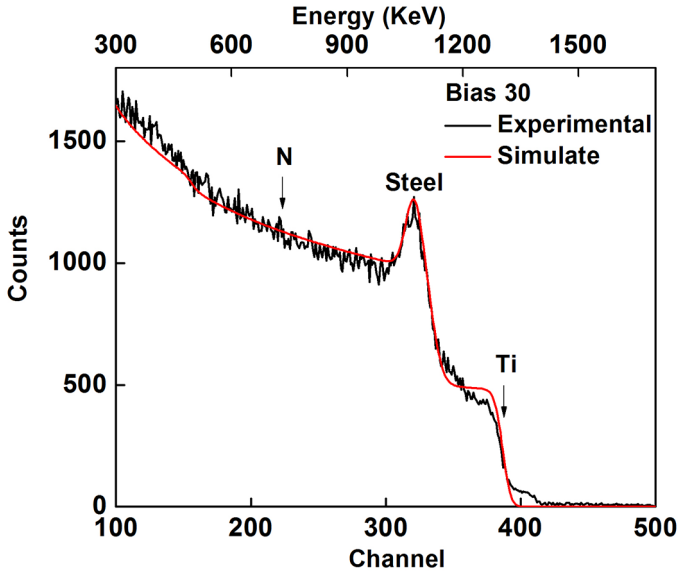

Fig. 3. Typical RBS spectrum of TiN film deposited at −30 V bias voltage.

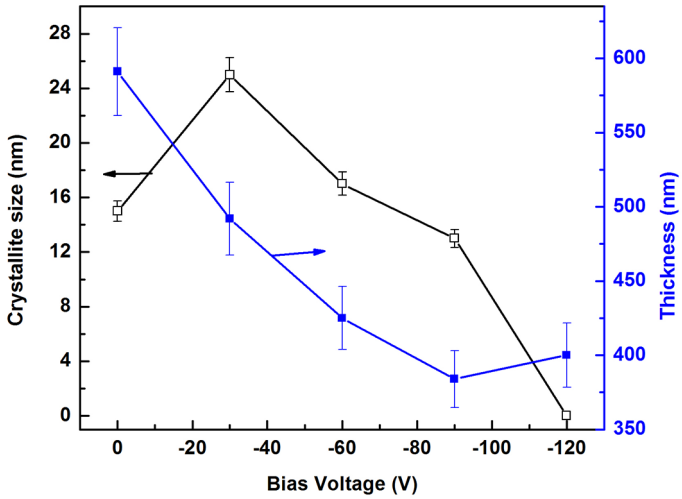

Fig. 4. Variation of (a) crystallite size and (b) film thickness with bias voltage.

RBS spectra; it is found that in all samples the ratio is close to 1, and thus illustrating a possible tendency for the formation of stoichiometric TiN film. The average crystallite size calculated from the Scherrer equation for preferred orientation [20] and the film thickness obtained from RBS analysis are depicted in fig. 4. It can be observed that a maximum crystallite size of about 24 nm is obtained at $|-30|$ V. Applying the $|-30|$ V voltage results in an increase of surface atom and grain boundary mobilities due to momentum transfer of the incident ions. Above −30 V, with increasing the incident ion energy toward the substrate, the number of defects as preferential nucleation sites as well as the etching of surface island edges could increase, having as a consequence a decrease in the crystallite size. The overall trend of thickness variation as a function of V_b appears to be a decreasing trend due to breaking the Ti-N bonds and also surface etching by impact of ions with higher energy.

The XPS survey spectrum of the film deposited at −30 V (fig. 5) exhibits the characteristic N 1s, Ti 2p and O 1s peaks at binding energies of 396.2, 456.5 and 528.2 eV, respectively. The binding energies of the observed peaks were calibrated respect to C 1s peak at 284.6 eV. The presence of carbon and oxygen peaks may be related to the environmental pollution of the surface. Deconvoluted Ti 2p and N 1s XPS spectra are shown in fig. 6. The high-resolution Ti 2p peak of the films displays the spin orbit splitting characteristics. The deconvoluted Ti 2p peak displays five component resolutions at the binding energies of 456, 457.3, 458.7, 459.9 and 461.1 eV corresponding to TiN [21–23], Ti_2O_3 [23], TiO_2 [24] and Ti [25] compounds, respectively. The N 1s peak position remains essentially unchanged at 396.2 [26], 397.6 [26,27] and 400 eV [28]. The most probable assignments to the components of the Ti 2p and N 1s peaks are presented in table 1.

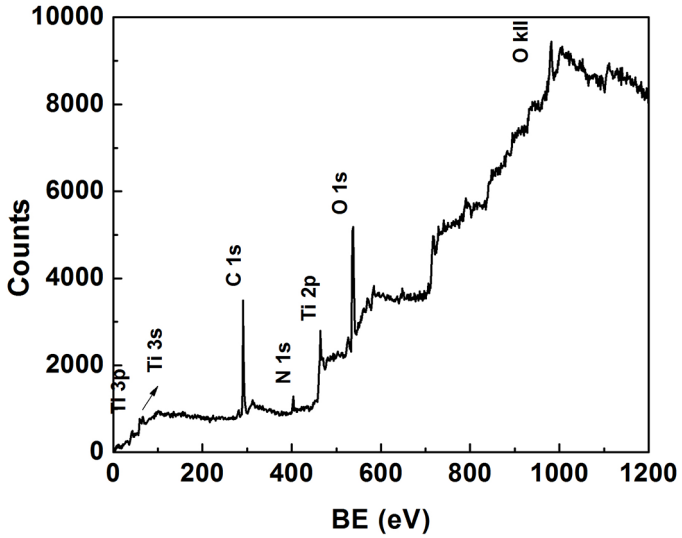

Fig. 5. XPS high-resolution spectra of the TiN film deposited at −30 V.

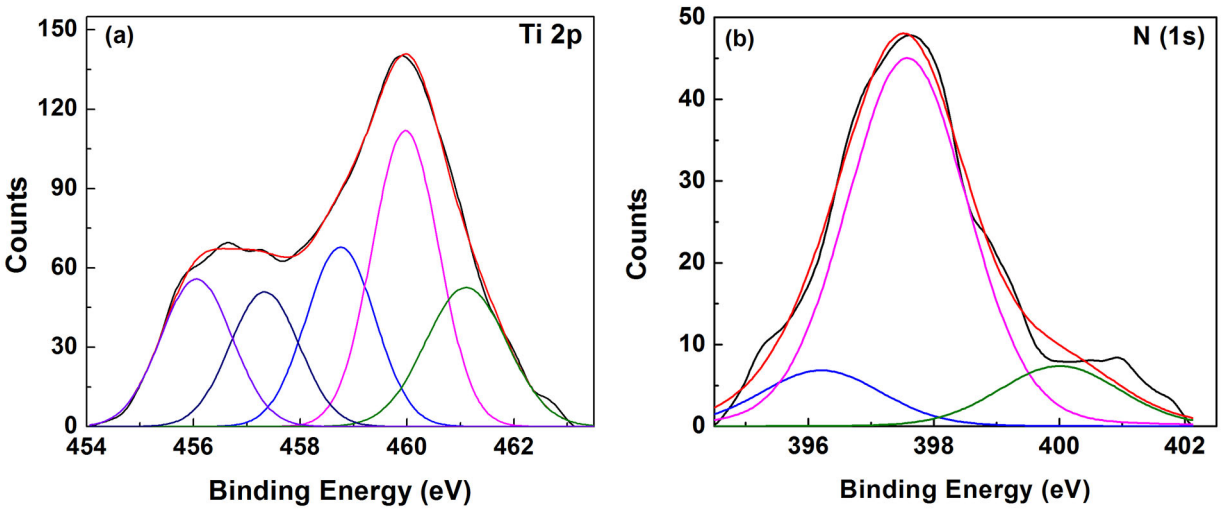

Fig. 6. The deconvoluted (a) Ti $2p_{3/2}$ and (b) N 1s XPS peaks.

Table 1. Assignments to peak components of high-resolution XPS scans of TiN film prepared at −30 V.

Peak	Component	Binding energy (eV)	Assignment	Ref.
Ti $2p_{1/2}$	I	461.1	TiN	[21]
Ti $2p_{3/2}$	IV	456	TiN	[21–23]
		457.3	Ti_2o_3	[23]
		458.7	TiO_2	[24]
	V	459.9	Metallic Ti	[25]
N 1s	I	396.2	TiON	[26]
		397.6	TiN	[26,27]
	II	400	N_2	[28]

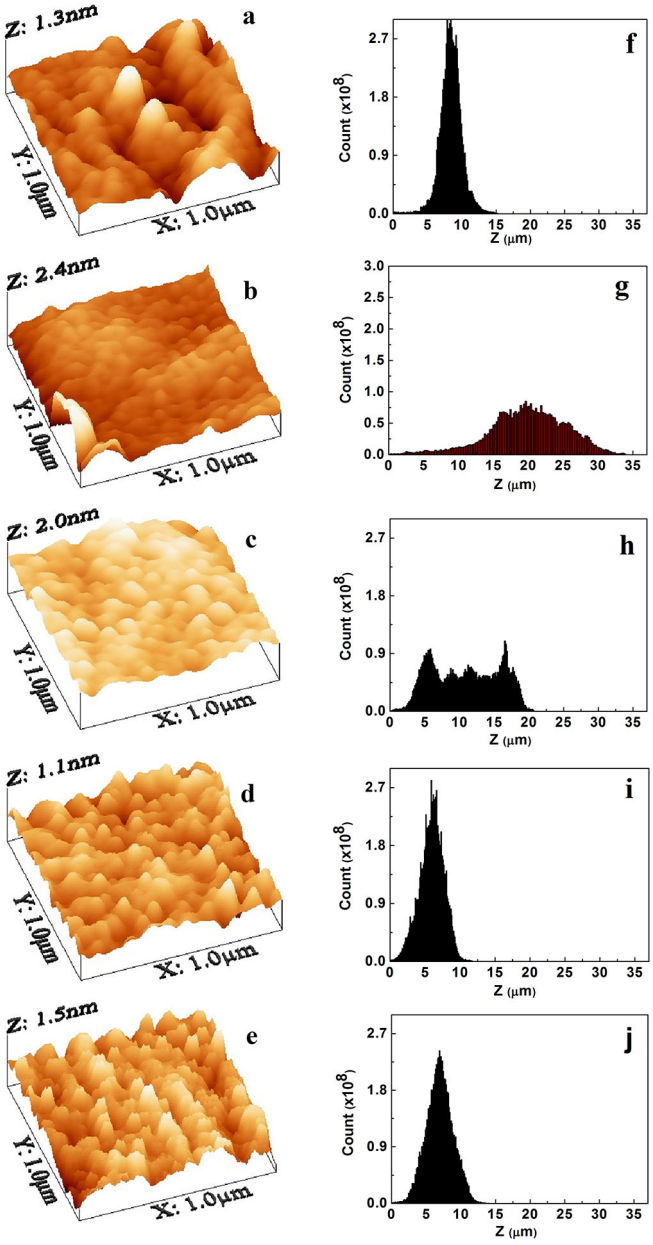

Fig. 7. 3D AFM images and height histogram of TiN films prepared at ((a), (f)), 0 ((b), (g)), −30 ((c), (h)), −60 ((d), (i)), −90 and ((e), (j)) −120 V bias voltages.

The detection of oxygen by XPS and not by RBS is certainly related with the RBS resolution when small content of light elements are involved (below 5 at %). On the base of i) the high quantity of TiN relative TiON, observable in fig. 6(b) (integrating the area under peak for TiN and TiON), ii) small amounts of oxygen according to RBS results and iii) the absence of the peak attributed to the TiON in XRD patterns which is a possible suggestion that the N 1s peak at $\sim$ 396 eV is not a characteristic peak of N 1s spectrum in the TiON ternary system. Moreover, due to the fact that XPS is a surface-sensitive technique because only those electrons generally near the surface escape and are detected (photoelectrons originating more than 20 to 50 Å below the surface cannot escape with sufficient energy to be detected), it can be inferred that the N 1s peak at 396 eV should result from the surface contamination. Similar results on TiN films were obtained by other authors [29,30].

The surface topography has been studied by $1 \times 1\,\mu m^2$ AFM images. The substrate shows an almost smooth surface (RMS $\sim$ 0.89 nm). The evolution of surface features with bias voltage is presented in 3D AFM images in fig. 7. The obtained data as RMS and full width half maximum (FWHM) of the histograms are tabulated in table 2. It seems that FWHM is also a proper parameter to describe surface roughness behavior of the films. The surface of film prepared at −30 V shows a bumpy topography created by relatively loosely packed columns and also larger

Table 2. RMS and FWHM of TiN films prepared at different bias voltages.

Bias (V)	RMS (nm)	FWHM
0	1.86	10.69
−30	5.53	11.97
−60	4.74	4.88
−90	1.74	3.86
−120	1.93	4.37

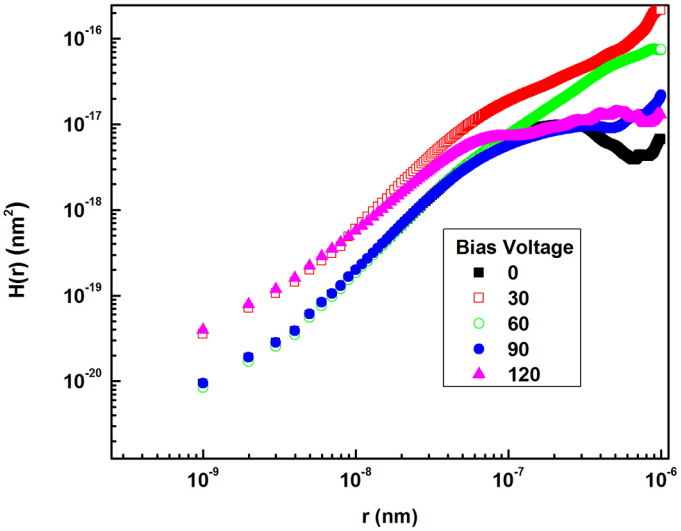

Fig. 8. Height-height correlation function as a function of film thickness.

grains with less voided boundaries compared with as-prepared sample ($V_b = 0\,V$). Above $-30\,V$, the films are clearly characterized by a pyramidal structure bordered by relatively narrow and deep channels. Variation of surface roughness with bias voltage is generally arisen from interbalance between the impaction energy, the number of nucleation sites and resputtering mechanism as three important factors.

To investigate the random and/or statistical ordering behavior of the deposition process, height-height correlation function (second-order statistical measuring, $H(r)$) from $N \times N$ ($N = 256$) AFM images is calculated. $H(r)$ as a function of position (r) in the scan direction (x-direction) is defined as follows [31]:

$$H(r = md) = \frac{1}{N(N-m)} \sum_{j=1}^{N} \sum_{i=1}^{N-m} (h(i+m, j) - h(i, j))^2, \tag{3}$$

in which d and $h(i, j)$ are the horizontal distance between adjacent image pixels and height of the surface measured at the (i, j) point of the AFM images, respectively. m was chosen to be 128 for all the samples. In the short-range region, the double logarithmic plot of $H(r)$ *versus* r is a straight line, whose slope determines the roughness exponent (α) which directly gives the fractal dimension by $FD = 3 - \alpha$, the larger α, the lower the surface roughness. The lateral correlation length is obtained through the $H(r)$ curve fitting as a form [32]

$$H(r) = 2(RMS)^2 \left(1 - \exp\left[-\left(\frac{r}{\zeta}\right)^{2\alpha}\right]\right). \tag{4}$$

The height-height correlation function curves of the samples are shown in fig. 8. Very close values of the roughness exponent ($\alpha \sim 0.7$) of the films implies similar dynamics of roughness growing of the surfaces during deposition process. Several experiments on self-affine films deposited by different techniques [33–36] showed that α ranges from 0.65 to 0.9, which are values higher than those predicted by non-conservative growth models, *i.e.* prediction of the KPZ equation (≤ 0.5). All RMS values have been corrected for the RMS width of the stainless steel substrate, according to

$$\mathrm{RMS}_{\mathrm{corrected}} = (\mathrm{RMS}^2 - \mathrm{RMS}_{\mathrm{ss}}{}^2)^{1/2}, \tag{5}$$

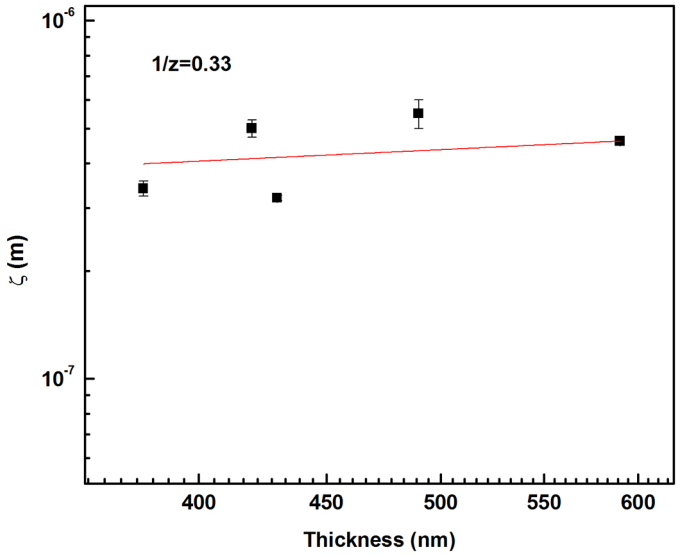

Fig. 9. Experimental values of the correlation length for TiN films as a function of film thickness.

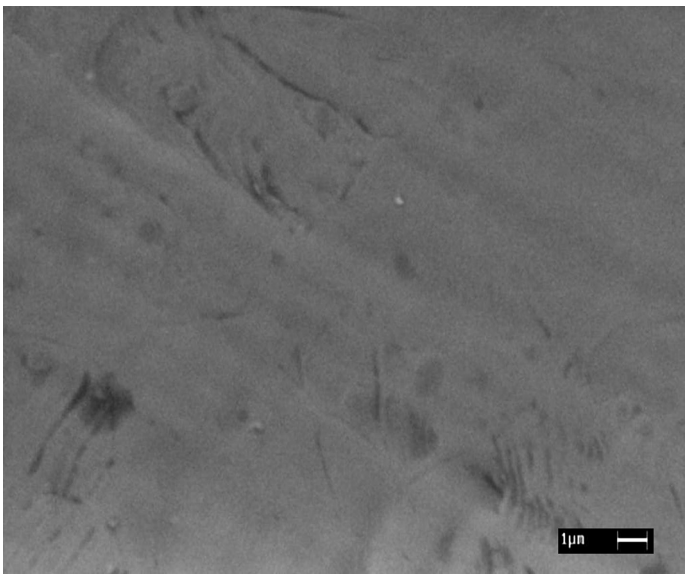

Fig. 10. SEM images of TiN films deposited at −30 V bias voltage.

which affected the reported β values less than 0.07. Figure 9 shows the double logarithmic plot of the correlation length as a function of the film thickness. The slope of the fitted curve as linear form presents dynamic scaling exponent of 3.03, which is in accordance with the previously obtained $z = 3.5$ ($z = \alpha/\beta$) and $\beta = 0.25$. Comparison of the obtained exponents with theory of non-equilibrium film growth [15,37] guide us to predict the atomistic deposition equation as follows:

$$\frac{\partial h}{\partial t} = \lambda_1 \nabla^2 (\nabla h)^2 + \eta - \kappa_1 (\nabla^4 h), \tag{6}$$

where η is a random function, whose mean value gives the average particle flux at each point and its fluctuations represent the shot noise in the deposition [38]. In this model atoms are continually coming onto the surface from the incident flux and subsequently relax to nearby kink sites maximizing the number of saturating bonds. As a result of theoretical studies supported by experimental data (see also fig. 10), a relative smooth growth would then be expected for all the films. The correlation lengths are observed to be one order greater than the crystallite size obtained from XRD patterns. This result is in accordance with theory but is different from obtained results in ref. [39].

The nanoindentation results for elastic modulus (E) and hardness (H) values of TiN films are presented in fig. 11. During the hardness test of thin films deposited on a bulk substrate, choosing the correct imprint depth is very important factor. On the other hand, to avoid the substrate effect on the film hardness values, the depth of the imprint should be much less than the film thickness ($\leq 20\%$). Therefore, the depth of 50 nm was used to measure

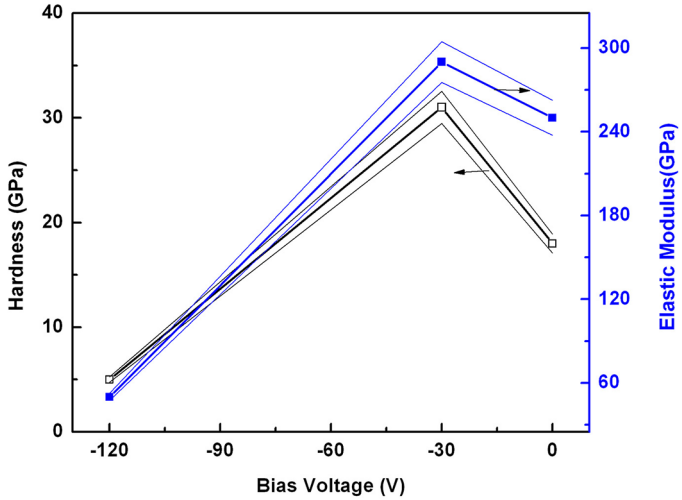

Fig. 11. Hardness and elastic modulus of TiN films as a function of bias voltage.

Table 3. Mechanical properties of TiN films prepared at different bias voltages.

Bias (V)	Hardness (GPa)	Elastic modulus (GPa)	H^3/E^2 (GPa)	Grain size (nm)
0	18	250	0.09	–
−30	31	290	0.35	26
−120	5	50	0.05	21

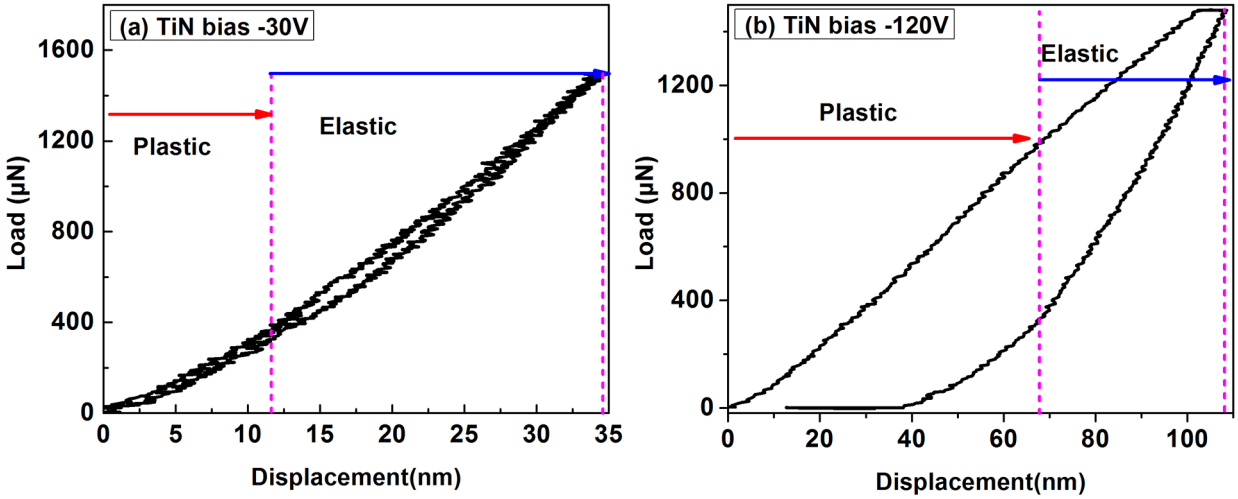

Fig. 12. Nanoindentation loading/unloading curves for TiN films prepared at bias voltage (a) −30 V and (b) −120 V bias voltages.

H and E values of the films. The hardness of substrate was evaluated to be about 3 GPa and the maximum load of 1.5 mN has been applied to measure the film hardness. As can be seen, H initially increases from 18 to 31 GPa as the bias voltage increases from 0 to −30 V. Further increase of bias voltage to −120 V considerably decreases H to 5 GPa. As explained before, increasing the incident ion energy by bias voltage can results in more defects, change in the film structure from crystalline to amorphous structure, leading to a decrease in the film hardness. The ratio of H^3/E^2 controls the resistance of materials to plastic deformation [37]. The plastic deformation possibility reduces for materials with high hardness and low modulus. In general, a low modulus is also desirable as it allows the given load to distribute over a wide area. Plastic deformation resistance values of the films are presented in table 3. The maximum H^3/E^2 ratio is obtained for the film prepared at −30 V. Figure 12 shows the load-displacement curves for the films prepared at −30 and −120 V. It is clear that the film prepared at −30 V has more elastic recovery and less plastic deformation than the film prepared at −120 V (66% compared to 39%). Comparison of two curves indicates that with a constant applied load, the maximum penetration depth increases with increasing the bias voltage from 35 nm for −30 V bias to 109 nm for −120 V bias, as a consequence of a decrease in the film hardness.

4 Conclusions

HCD-IP method was used to deposit TiN thin films onto 316 stainless steel substrate by variation of bias voltage. The films were grown in preferential crystalline direction of (200). The film deposited at −30 V possessed the highest hardness (~ 30 GPa) and elastic modulus (290 GPa). AFM was employed to quantitative investigation of the kinetic surface-roughening phenomenon of the deposited TiN thin films. Surface scaling analyses from the RMS roughness and the height-height correlation function $H(r)$ showed that the surface growth of TiN thin films can be theoretically predicted by statistical growth models. Statistical evaluation of dynamic scaling behavior of the films revealed similar roughness growing of the films. The roughness, growth and dynamic scaling exponents have been independently measured ($\alpha = 0.7 \pm 0.05$, $\beta = 0.25 \pm 0.05$ and $z = 3.03 \pm 0.05$). Comparison of the obtained exponents with theory of non-equilibrium film growth predicts a smooth growth in agreement with experimental growth.

References

1. W.D. Sproul, Thin Solid Films **107**, 141 (1983).
2. P. Honor, R. Sanjines, F. Levy, Surf. Coat. Technol. **94–95**, 398 (1997).
3. J.W. Lim, J.S. Park, S.W. Kang, Appl. Phys. **87**, 4632 (2000).
4. J.F. Marco, J.R. Gancedo, M.A. Auger, O. Sanchez, J.M. Albella, Surf. Interface Anal. **37**, 1082 (2005).
5. R. Hübler, A. Cozza, T.L. Marcondes, R.B. Souza, F.F. Fiori, Surf. Coat. Technol. **142–144**, 1078 (2001).
6. M. Flores, S. Muhl, E. Andrade, Thin Solid films **433**, 217 (2003).
7. A.J. Aronson, D. Chen, W.H. Class, Thin Solid films **72**, 535 (1980).
8. A. Armigliato, M. Finetti, J. Garrido, S. Guerri, P. Ostoja, A. Scorzoni, J. Vac. Sci. Technol. A **3**, 2237 (1985).
9. W.-J. Chou, G.-P. Yu, J.-H. Huang, Surf. Coat. Technol. **140**, 1206 (2001).
10. J.M. Lackner, W. Waldhauser, R. Berghauser, R. Ebner, B. Major, T. Schoberl, Thin Solid films **453-454**, 195 (2004).
11. W.-J. Chou, G.-P. Yu, J.H. Huang, Surf. Coat. Technol. **149**, 7 (2002).
12. N. Saqula, K. Henda, R. Kesri, Plasma Fusion Res. **8**, 1403 (2009).
13. P. Meakin, Phys. Rep. **235**, 189 (1993).
14. T. Halpin-Healy, Y.C. Zhang, Phys. Rep. **254**, 215 (1995).
15. A.-L. Barabasi, H.E. Stanley, *Fractal Concepts in Surface Growth* (Cambridge University Press, Cambridge, England, 1995).
16. M. Kardar, Physica A **281**, 295 (2000).
17. M. Cattani, M.C. Salvadori, Thin Solid Films **376**, 264 (2000).
18. M. Kardar, G. Parisi, Y.-C. Zhang, Phys. Rev. Lett. **56**, 889 (1986).
19. M. Siegret, M. Plishke, Phys. Rev. Lett. **73**, 1517 (1994).
20. A. Monshi, M.R. Foroughi, M. Monshi, R. Worl, Nano. Sci. Eng. **2**, 154 (2012).
21. C.W. Zou, H.J. Wang, M. Li, Y.F. Yu, C.S. Liu, L.P. Guo, D. Fu, Vacuum **84**, 817 (2010).
22. J.T. Chen, J. Wang, F. Zhang, G.A. Zhang, X.Y. Fan, Z.G. Wu, P.X. Yan, J. Alloy. Compd. **472**, 91 (2009).
23. S. Rtimi, O. Baghriche, C. Pulgarin, R. Sanjinesb, J. Kiwi, RSC Adv. **2**, 8591 (2012).
24. E. Simonsen, E. Morten, J.H. Li, G. Zheshen, E. Soagaarda, Photochem. Photobiol. A **200**, 192 (2008).
25. W. Wu, X.H. LIU, Y.D. Huimin, S. Lu, Mater. Sci. Technol. **24**, 145 (2008).
26. F.-H. Lu, H.-Y. Chen, Surf. Coat. Technol. **130**, 290 (2000).
27. F.-H. Lu, H.-Y. Chen, Thin Solid Films **355-356**, 374 (1999).
28. J. Yang, H. Bai, Q. Jiang, J. Lian, Thin Solid Films **516**, 1736 (2008).
29. C. Emsberger, J. Nickerson, A.E. Miller, J. Moulder, J. Vac. Sci. Technol. A **3**, 2415 (1985).
30. J. Vasile, A.B. Emerson, F.A. Baiocchi, J. Vac. Sci. Technol. A **8**, 99 (1990).
31. D. Raoufi, A. Kiasatpour, H.R. Fallah, A.S.H. Rozatian, Appl. Surf. Sci. **253**, 9085 (2007).
32. E.S. Gadelmawla, M.M. Koura, T.M.A. Maksoud, I.M. Elewa, H.H. Soliman, Mater. Proc. Technol. **123**, 133 (2002).
33. R.P. Chiarello, V. Panella, J. Krim, C. Thompson, Phys. Rev. Lett. **67**, 3408 (1991).
34. M.W. Mitchell, A. Bonell, Mater. Res. **5**, 2244 (1990).
35. J.M. Gómez-Rodriguez, A.M. Baró, R.C. Salvezza, J. Vac. Sci. Technol. B **9**, 495 (1991).
36. F. Ruffino, M.G. Giannazzo, F. Roccaforte, V. Raineri, Nanoscale Res. Lett. **4**, 262 (2006).
37. Z.W. Lai, S.D. Sarma, Phys. Rev. Lett. **66**, 2348 (1991).
38. M. Kardar, Physica B **221**, 60 (1996).
39. G. Palasantzas, J. Krim, Phys. Rev. Lett. **73**, 3564 (1994).